Published in final edited form as:

Macromol Chem Phys. 2021 April ; 222(7): . doi:10.1002/macp.202170013.

Silk Film Stiffness Modulates Corneal Epithelial Cell Mechanosignaling

M. G. Sun[a,b], **Y. Luo**[a], **T. Teng**[b], **Dr. V. Guaiquil, PhD**[a], **Dr. Q. Zhou, MD, PhD**[a], **L. McGinn**[a], **O. Nazzal**[c], **Dr. M. Walsh, PhD**[d], **Dr. J. Lee, PhD**[b], **Dr. M. I. Rosenblatt, MD, PhD, MBA**[a]

[a]Department of Ophthalmology and Visual Sciences, University of Illinois at Chicago, 1855 W. Taylor St., Chicago, IL 60612

[b]Department of Bioengineering, University of Illinois at Chicago, 851 S. Morgan St., Chicago, IL 60607

[c]Department of Pathology, University of Illinois at Chicago, 840 S. Wood St., Suite 130 CSN, Chicago, IL 60612

[d]Department of Material Sciences and Engineering, University of Wisconsin - Eau Claire, 101 Roosevelt Ave., Eau Claire, WI 54701

Abstract

Silk fibroin films are excellent candidate biomaterials for corneal tissue engineering due to their optical transparency, biocompatibility, and mechanical strength. Their tunable chemical and mechanical properties open the possibility of engineering cellular microenvironments that can both mimic native corneal tissue and provide stimuli to actively promote wound regeneration. While silk film mechanical properties, such as surface topography, have demonstrated the ability to control corneal epithelial cell wound regenerating behavior, few studies have explored the stiffness tunability of these films and its cellular effects. Cells are known actively sense the stiffness of their surroundings and processes such as cell adhesion, migration, proliferation, and expression of stem markers can be strongly influenced by matrix stiffness. This study develops technical solutions that allow for both the fabrication of films with stiffnesses similar to corneal tissue and also for their characterization in an aqueous, native-like environment at a scale relevant to cellular forces. Physiological evidence demonstrates that corneal epithelial cells are mechanosensitive to films of different stiffnesses and show that cell spreading, cytoskeletal tension, and molecular mechanotransducer localization are associated with film stiffness. These results indicate that silk film stiffness can be used to regulate cell behavior for the purposes of ocular surface repair.

Keywords

silk fibroin film; atomic force microscopy; Young’s modulus; mechanotransduction

*(corresponding author) mrosenbl@uic.edu.

CONFLICT OF INTEREST

The authors declare no conflicts of interest.

1. INTRODUCTION

Silk fibroin, extracted from the *Bombyx mori* silkworm, is a versatile protein that can be processed into various biomaterial forms such as films, hydrogels, sponges, nanoparticles, and electrospun fibers. Films cast from the fibroin solution are particularly well-suited for corneal tissue engineering and ocular surface repair due to their optical transparency, mechanical strength, and biocompatibility.[1, 2] Additionally, the chemical and mechanical properties of these films are highly tunable which provides the ability to engineer films with specific biochemical and physical stimuli that can actively accelerate cellular wound healing. For example, chemical modifications, such as the incorporation of poly-D-lysine (PDL) and arginine-glycine-aspartic acid (RGD) peptides [3] or blending of extracellular matrix (ECM) into the silk structure [4] have been shown to improve critical wound healing processes such as cell adhesion, migration, and proliferation. Multiple groups, including our own, have also demonstrated that silk films can be patterning via soft lithography techniques and that the nanotopographies of these films can improve adhesion, migration, proliferation, and the expression of stem cell markers in corneal cells.[5–8]

It is well known that the stiffness of the cellular microenvironment can have profound effects on many cellular processes. For example, matrix stiffness has been shown to dictate mesenchymal stem cell lineage fate and play an integral role in embryonic development.[9, 10] Mismatched stiffness of a biomaterial implant and its tissue have been associated with promoting foreign body reactions [11, 12] and implant failure,[13] while aberrantly increased tissue stiffness has been suggested to act as a stimulus for disease progression in cancer and fibrosis.[14, 15] In the cornea, Gouveia et al. have recently demonstrated the importance of in vivo tissue stiffness on limbal stem cell phenotype and wound healing.[16] Their study indicated that limbal stem cells are sensitive to the stiffness of their surrounding matrix and demonstrated a loss of stem cell markers on stiffened corneas wounded by alkali burn. Collectively, these findings indicate that the stiffness of the cellular environment is a powerful mechanical stimulus that can have profound effects on cellular behaviors crucial for wound recovery.

While tunable biomaterials like silk fibroin films offer an excellent means to engineer the stiffness of a cell's microenvironment, there are a lack of studies reporting on how to control the stiffness of these films and its resulting effects on corneal cell behavior. Available studies evaluating silk film stiffness characterize only the material's bulk properties rather than that of the material's surface. While both bulk and surface properties are essential for biomaterial design, they can differ greatly from one another.[17, 18] Bulk material properties indicate how a material will behave under macroscopic forces and is important in factors such as suture strength and load bearing ability. In contrast, surface material properties define the biophysical cues at the cell-material interface and are thus primarily responsible for how cells respond to a material.[17, 19–22] While studies have used atomic force microscopy (AFM) to characterize the surface properties of silk films on a scale relevant to cellular mechanical forces,[23–29] only dried films have been evaluated. The mechanical properties of dried silk films differ substantially from fully hydrated films [27] in an aqueous environment like that of the cornea, and therefore, are unrepresentative of the biophysical cues present to cells.

In this study, we were able to develop novel technical solutions that allowed for the tuning of silk film stiffnesses within the physiological range of native corneal tissue and also for their characterization via AFM in an aqueous environment like that of the cornea. Additionally, we provide evidence that advance our understanding on the physiological response of corneal epithelial cells to silk film surface stiffness. We demonstrate that cell spreading, actin cytoskeletal tension, and signaling of the mechanosensing molecule yes-associated protein (YAP) were all significantly affected by film stiffnesses. We believe that the regulation of silk film stiffness and an understanding of its effects on corneal cell behavior will be important for applications in ocular surface repair.

2. METHODS

2.1. Preparation of Silk Fibroin Solution

Extraction of silk fibroin was performed according to previously described protocol.[8] Briefly, cocoons from *Bombyx mori* silkworms (Tajima Shoji Co., Yokohama, Japan) were cut into fourths and boiled in Na_2CO_3 alkaline solution (0.02 M) for 40 minutes to remove sericin proteins. The boiled fibers were washed with distilled water and allowed to dry overnight in ambient conditions. The fibers were dissolved in LiBr (9.3 M) for 4 hours at 60°C. The solution was then dialyzed (MWCO 3,500) in deionized water for 48 hours to extract the LiBr. The dialyzed solution was centrifuged at 10,000 g at 4°C and the supernatant was collected and stored at 4°C.

2.2. Casting Silk Fibroin Solution onto Plasma-Treated Polyester

Surface modification through plasma treatment is commonly used to improve material adhesion and hydrophilicity.[30] Before casting silk fibroin solution to create films, we treated 15 mm round polyester Thermanox™ coverslips (Fisher Scientific, Hampton, NH) with oxygen plasma in a PE-50 benchtop plasma cleaning system (PlasmaEtch, Carson City, NV). The coverslips were individually laid on a flat platform, and one surface was exposed to oxygen plasma (~10 cc min^{-1}) for 5 minutes under vacuum (200 mTorr). Silk films were then made by casting 8% wt vol^{-1} silk fibroin solution (70 μl) onto the plasma-treated coverslips and allowed to dry overnight. All solutions were cast onto the coverslips within 10 minutes of oxygen plasma treatment. Dried films were placed into 24-well plates and annealed in methanol (MeOH) for 90 minutes to induce β-sheet formation (0.5 mL). MeOH-annealing concentration was varied from 30, 40, 50, and 60% vol (hereafter referred to as 30%, 40%, 50%, and 60% films). MeOH was then removed and films were thoroughly washed overnight in distilled water prior to use.

2.3. Atomic Force Microscopy Nanoindentation

Silk film stiffness and topography was assessed using an MFP-3D-BIO (Asylum Research, Goleta, CA) atomic force microscope. MeOH-annealed films on plasma-treated cover slips were first adhered to glass slides using a waterproof polyurethane contact adhesive (Gorilla Glue, Cincinnati, OH). The adhesive was applied between the cover slip and glass slide, and care was taken to avoid contact with the silk film sample. Films were hydrated and submerged in phosphate buffer saline (PBS) prior to analysis. For stiffness measurements, silk films annealed with 30% and 40% MeOH were indented using a 0.75 N m^{-1} spring

constant TR800PB silicon nitride probe while 50% and 60% films were indented with a 1.85 N m^{-1} AC240TS-R3 silicon probe (Asylum Research, Goleta, CA). Prior to indentation, the InvOLS and spring constant of each probe were calibrated on glass substrates. For each sample, 12 measurements were taken in different regions of the film at an indentation speed of 1.0 μm s^{-1} and a trigger point of 50.0 nm deflection. This was repeated for three samples from separate experiments to account for batch variation. The Young's modulus was determined by fitting of stress-strain force curves with linear Young's Hertzian contact model.

2.4. Atomic Force Microscopy Topography Imaging

For surface topography imaging of silk films in a native aqueous environment, TR400PSA silicon nitride probes were used for all MeOH-annealing conditions and operated using AFM non-contact mode. A 20 × 20 μm area was scanned at an XY velocity of 0.25 Hz scan rate for each sample. Each image consisted of 512 pixels along the scanning path and 256 pixels in the direction perpendicular. For quantification of the film topography, images were first corrected using Gwyddion software (v2.55). Leveling was performed on all images by fitting and subtraction of a 5^{th} order polynomial. Horizontal lines resulting from imaging artifacts were also removed. Spectral analysis was performed in Matlab software where the one-dimensional (1D) profiles along the scanning path (512 pixels) were decomposed into their constitutive frequencies using 1D Fourier transforms. The power spectrum was computed by taking the squared magnitude of each Fourier coefficient. The power spectral density (PSD) for each film was determined by averaging the power spectrum calculated at 100 separate lines in the direction perpendicular to the scanning path. The ABC or k-correlation model was fitted to the PSD of each film using the least squares method (Equation 1). Model parameters A, B, and C were used to calculate the root-mean-square (RMS) roughness (Equation 2) and correlation length (Equation 3) which corresponds to the average grain size. This was repeated for three samples from separate experiments to account for batch variation.

2.5. Scanning Electron Microscopy

SEM was used to assess the topography of dehydrated MeOH-annealed silk films. Silk films were fixed in of Karnovsky's fixative (400 μL) for 50 minutes at room temperature and washed three times in PBS. The films were then dehydrated in a series of ethanol concentrations (50%, 80%, 90%, and 100%), for 7 minutes each. Films were then further dried using hexamethyldisiloxane (HMDS; Sigma-Aldrich) solvent to remove residual water saturation for 2 minutes and then allowed to dry overnight in a desiccator. Prior to SEM imaging, the films were sputter coated with gold for 90 seconds, leaving a thin layer on the sample surface. Films were imaged using a JSM-6320F SEM (JEOL USA, Inc., Peabody, MA).

2.6. Fourier-Transform Infrared Spectroscopy

Silk film secondary structure was analyzed using a Cary 630 FTIR Spectrometer (Agilent Technologies, Santa Clara, CA) equipped with an attenuated total reflectance (ATR) diamond crystal. Spectral scans were performed on dried 30%, 40%, 50%, and 60% MeOH-annealed films to examine changes in secondary structure in response to increasing MeOH

concentrations. Six samples were tested per condition where 1000 scans were co-added and averaged at a resolution of 4 cm^{-1} and over a wavenumber range of 650– 4000 cm^{-1}. FTIR spectra were pre-processed in Origin Lab (2019 version). Baseline correction was performed using the 2nd derivative method where anchor points were first chosen manually and connected by interpolation. Subtraction of the baseline was performed to obtain the baseline-corrected spectrum. Finally, secondary structures were assigned to wavenumber positions according to previously reported studies: random coils at 1640–1650 cm^{-1} and β-sheets at 1610–1625 cm^{-1}.[31, 32]

2.7. Thermogravimetric Analysis

Silk film water content was assessed using a TA Q5000 thermogravimetric analyzer (TA Instruments, Wood Dale, IL). MeOH-annealed films were hydrated in dH_2O prior to analysis. A 5 mm trephine was used to create small punches of each sample. Any adsorbed liquid on the film surface was removed by wiping against the sample container prior to loading into a TGA aluminum pan (TA Instruments, Wood Dale, IL). Samples were heated from room temperature to 400°C at a rate of 10°C min^{-1} in an inert nitrogen atmosphere with a purge flow rate of 40 mL min^{-1}. Silk film water content was assessed by observing the percent of initial weight at the first plateau region in the weight loss profiles. This technique has previously been reported for analysis of silk film water content.[33] TGA analysis was performed on three samples per condition from separate experiments to account for batch variation. Data were normalized to initial weight values.

2.8. Cell Spreading Analysis

The human corneal limbal epithelial (HCLE) cell line, kindly provided by Ilene Gipson, PhD., was used as a model for assessing the effects of substrate stiffness on corneal epithelial cell behavior. HCLE cells were plated on 30%, 40%, 50%, and 60% MeOH-annealed films at a density of 5,000 cells per film in keratinocyte serum-free (KSF) media (EGF, BPE, 1% P/S, and 1% AA). Cells were incubated at 37°C and 5% CO_2 for 24 hours and then imaged using phase contrast microscopy with a 10x objective (ZEISS, Germany). Cell area analysis was performed by manually tracing individual cells (ZEN 2.1, ZEISS, Germany). The experiment was repeated three times with 100 cells areas taken per replicate.

2.9. Immunostaining

For fluorescent imaging, silk films were cast onto 15 mm plasma-treated glass coverslips as plastic Thermanox™ coverslips exhibit autofluorescence. HCLE cells were cultured on 30%, 40%, 50%, and 60% MeOH-annealed films at a density of 9,000 cells per film in KSF media (EGF, BPE, 1% P/S, and 1% AA). Cells were incubated at 37°C and 5% CO_2 for 24 hours. Cells were fixed in 4% PFA, permeabilized with 0.5% Triton X-100, and stained with Rb YAP (Cell Signaling cat #14074) and phalloidin-conjugated 568, both at a 1:100 dilution. The samples were mounted using Vectashield® antifade mounting medium (Vector Labs, Burlingame, CA). For the localization of YAP, images taken with fluorescent microscope using 10x objective (ZEISS, Germany). HCLE cells were categorized based on the localization of YAP protein as exhibiting either “predominant nuclear localization,” “predominant cytoplasmic localization,” or “equal nuclear/cytoplasmic distribution” as seen in previously published studies.[34–37] Results are represented as a percentage of cell

population with predominantly nuclear YAP distribution. YAP analysis was repeated with three films per condition.

2.10. Statistical Analysis

All statistical analysis was performed using GraphPad Prism. *A priori* testing for normality was done using the D'Agostino-Pearson test. Differences in means were analyzed using the Kruskal-Wallis test with post hoc multiple comparisons for all nonparametric data. Dunn's test was performed to correct for multiple comparisons. Significance was determined as $p < 0.05$ for all experiments. Simple linear regression was performed for individual analysis of the log of the Young's modulus, RMS roughness, and correlation length with the cell spreading area as the dependent variable for each model.

3. RESULTS & DISCUSSION

3.1. Oxygen plasma enables adhesion of hydrated silk films and allows for AFM characterization in a native-like environment

AFM is a powerful tool that is commonly used to characterize the mechanical properties of biomaterials. Compared to techniques that measure bulk material properties on a macroscopic scale, such as tensile and compressive testing, AFM is able to evaluate a material's surface at a nanoscopic level. Forces on this magnitude are much more representative of what is experienced by cells at the cell-material interface. While studies have been published using AFM to measure the stiffness of silk films, to our knowledge, only dry films have been evaluated with stiffness values reported in the gigapascal (GPa) range.[23–29] These values are at least two orders of magnitude greater than the stiffness of most physiologic tissues which typically measure in the kilopascals (kPa). The mechanical properties of silk films are known to change dramatically from a glass-like, brittle state when dry to soft and highly flexible when fully hydrated.[33] We therefore argue that AFM studies on dry silk films are not representative of films in an aqueous environment such as that of the cornea and do not provide adequate information of the biophysical cues present to cells. The lack of AFM studies evaluating silk films in an aqueous environment is likely a result of technical difficulties in measuring thin film samples in a liquid. Stable sample adhesion is a requisite for accurate AFM measurements as any sample movement can cause significant errors. However, adhesion of thin tissues and hydrated films is typically challenging because many traditional adhesives such as cyanoacrylate glues cannot maintain adhesion when a sample is wet or submerged in liquid, as in the case of hydrated silk films. In addition, these adhesives can directly affect the hydration of thin samples due their hydrophobic mechanism of adhesion and can consequently alter the stiffness of the sample.

To overcome these obstacles and be able to study the biophysical cues of silk films in an aqueous environment representative of the cornea, we developed a novel technical solution for stable adhesion of thin film samples. Silk films were cast directly onto oxygen plasma-treated polyester coverslips (Figure 1a–c).

Oxygen plasma treatment of polyester induces the formation of hydrophilic oxygen-based functional groups at the polyester material surface.[30, 38, 39] We theorized that hydrophilic

activation of the polyester coverslips would increase the surface energy enough to allow for the silk films to strongly adhere. To support this theory, we observed that all silk films maintained stable adhesion to the plasma-treated coverslips throughout all aqueous processing steps including methanol (MeOH) annealing, AFM characterization in liquid, and cell culture. It is likely that the hydrophilic modification of the plasma treatment allowed for the formation of fibroin-polyester hydrogen and possibly covalent bonds. While the adhesion strength was not directly quantified, it was clear that casting silk fibroin films on plasma-treated polyester provided superior adhesive strength and stability compared to other methods. Some of the many methods we explored included adhesion with chrome-alum gelatin, fibrin glue, cyanoacrylate glues, double-sided tapes, and immobilization with mechanical devices, magnetic plates, and vacuum suction. The plasma technique also benefits from its ease of application and the minimal effects it has on silk film material properties compared with the other techniques explored. It should also be indicated that plasma treatment of glass coverslips did not produce adequate adhesion for AFM studies. Once the films cast onto plasma-treated glass were submerged in liquid and fully hydrated, they easily detached from the surface of the coverslip. In contrast, even after weeks of liquid immersion, the silk films did not detach from the plasma-treated polyester coverslips and were still adhered firmly. Finally, it should be noted that although the duration of the plasma-induced hydrophilic changes on the surface of the polyester coverslips was not measured, it appeared more difficult to spread the fibroin solution across the surface of the coverslips after around 30 minutes from plasma treatment, and therefore, solutions should be cast within this period. We speculate that this method of casting onto plasma-treated polyester coverslips may be applicable to other thin film samples that have previously proved difficult to characterize using AFM, though further studies are required to assess this claim.

3.2. Stiffness of silk films can be controlled using methanol processing

Using biomaterials to engineer the stiffness of a cell's microenvironment has the ability to induce significant changes in cellular behavior that can be exploited for therapeutic purposes.[36, 40] While the tunability of other silk film mechanical properties, such as its surface topography, have already demonstrated the ability to promote cellular wound regeneration, few studies are available that examine the regulation of silk film stiffness for the purposes of controlling cell behavior. To address this gap in the literature, various processing methods were tested to determine if any could control the stiffness of silk films. We found that MeOH-annealing was a simple and already utilized technique of silk film processing that could be modified to produce films with a wide range of stiffnesses. MeOH is known to induce physical crosslinking of the fibroin polymer chain through conformational changes from water-soluble random coils to water-stable β-sheet crystalline secondary structures.[41] By manipulating the concentrations of MeOH used for annealing, silk films could be produced with stiffnesses in the kilopascals, similar to that of corneal tissue.

To produce silk films with a wide range of stiffnesses, films were annealed with MeOH concentrations of 30%, 40%, 50% and 60% (Figure 2). All films appeared similar under

phase-contrast imaging (Figure 2b), although it should be noted that a slight decrease in transparency was observed as MeOH-annealing concentrations were lowered (Figure 2a).

We speculate that this may be related to a more disorganized structure of the fibroin polymer due to decreased β-sheet organization from partial MeOH-annealing. We believe that films with decreased transparency are still a viable option for corneal scaffolds because they are intended as temporary substrates that will eventually degrade and be replaced by native corneal tissue. Additionally, as there have been concerns with the biocompatibility of materials processed with MeOH, we argue that films annealed with reduced MeOH concentrations may improve biocompatibility, though assessment of this claim is needed. Nevertheless, all films were thoroughly washed after MeOH processing and prior to any cell studies. It should also be mentioned that annealing with concentrations lower than 30% MeOH produced unstable, gel-like films, likely due to inadequate crosslinking. To characterize the stiffness of hydrated MeOH-annealed silk films in an aqueous environment, films were first cast via the technique described previously, and AFM nanoindentation was operated in liquid, force contact mode. The Young's modulus, a measure of material stiffness, was generated by fitting the AFM force curves with the elastic Hertzian contact model. Silk films annealed with 30%, 40%, 50%, and 60% MeOH produced Young' moduli of 13.4 ± 5.4 kPa, 40.9 ± 20.38 kPa, 128.9 ± 37.5 kPa, and 445.4 ± 138.7 kPa (mean ± SD), respectively (Figure 3). Statistical analysis indicated strong significance and showed a clear trend between increasing MeOH concentrations and stiffer films.

To compare the stiffnesses of our MeOH-annealed films with reported AFM measurements of human corneal tissue, we turn to several studies in the literature. Last et al. evaluated the Young's modulus of individual layers of the human cornea using AFM and reported values of 7.5 ± 4.2 kPa (mean ± SD) for the anterior basement membrane, 33.1 ± 6.1 kPa for the anterior stroma, 50 ± 17.8 kPa for Descemet's membrane, and 109.8 ± 13.2 kPa for Bowman's layer.[42] Other AFM studies have reported Young's moduli measuring in the megapascals when evaluating human corneal stromas after epithelial debridement.[43–45] Variations in measurements can arise from many factors including AFM mounting procedure, sample preparation, and hydration of the tissue. Nevertheless, while measurements in the megapascal range are greater than our 30%−60% MeOH-annealed films, the Young's moduli described by Last et al. compare closely to our films. This indicates that MeOH-annealing has the potential to produce silk films within the stiffness of human corneal tissue.

We additionally sought to compare our AFM measurements with bulk material measurements of silk films annealed with similar concentrations of MeOH. A study by Lawrence et al. performing uniaxial tensile testing of fully hydrated silk films annealed in 50% MeOH reported Young's moduli of 21.97 ± 1.52 MPa (mean ± SD). When compared to the films annealed with the same MeOH concentrations measuring 128.9 ± 37.5 kPa from our study, the bulk material stiffness is nearly a magnitude higher than the surface stiffness of the films measured by nanoindentation. This comparison highlights the discrepancies between bulk and surface properties of a material and emphasizes that bulk properties may not be representative of those present at a material's surface. As cells can have significantly different responses on substrates that differ in stiffness by an order of magnitude, this is an

important consideration when engineering biomaterials that are intended to mimic the tissue microenvironment. Biomaterials with contrasting bulk and surface stiffness may be useful in replicating tissues with highly heterogeneous mechanical properties. For example, articular cartilage has been shown to display a steeply depth-dependent increase in tissue stiffness.[46–48] The superficial layer of articular cartilage is considerably softer than that of its bulk due to its intended role as a joint lubricant. Materials such as MeOH-annealed silk films may serve a unique role in creating scaffolds that mimic this tissue inhomogeneity.

3.3. Silk film β-Sheet density is directly related to its stiffness while water content is inversely related

Once silk films of varying stiffnesses could be produced, we sought to characterize the differences in their material properties. In particular, two properties known to significantly affect the Young's modulus of silk films are its β-sheet crosslinking density and its water content. MeOH annealing induces physical crosslinking of the silk fibroin polymer through the formation of β-sheet secondary structures.[41] The degree of β-sheet crosslinking is primarily responsible for the mechanical strength of these films, and therefore, we presumed that the range of Young's moduli observed in the AFM results correlated directly with silk film β-sheet content. To assess this theory, FTIR-ATR spectroscopy was performed. FTIR-ATR can determine a material's secondary structure composition by evaluating its absorption spectra of infrared light.[32, 33, 49] Spectral analysis was performed for all MeOH-annealing concentrations (Figure 4), and secondary structures were assigned to wavenumbers according to studies published by Hu et al.[31, 32] Our results revealed that peaks at wavenumbers corresponding to β-sheet structures (1610–1625 cm^{-1}) increased as MeOH concentrations increased, while no peaks were observed in the region of random-coils (1640–1650 cm^{-1}) for any MeOH concentrations. These results are consistent with previous reports where MeOH annealing was shown to primarily induce β-sheet crosslinking and confirm our theory that silk film stiffness is directly related to its β-sheet content.

As described, silk films dramatically change their mechanical properties when fully hydrated.[33] Water is known to plasticize the fibroin polymer which results in greater mobility, flexibility, and extensibility of silk fibroin films.[50] AFM studies performed on dry films report gigapascal Young's moduli,[23–29] similar to that of tissue culture plastic. In stark contrast, fully hydrated films from our study measured within kilopascals which is not only much more similar to the stiffness of physiological tissue, it is lower by two orders of magnitude. In order to investigate the relationship between water content and MeOH-annealing concentration, TGA was used to evaluate the mass loss profiles of hydrated silk films in response to increasing temperature (Figure 5). The mass loss occurring between 30°C - 60°C corresponds to water evaporation, and by assessing the mass remaining in the following plateau between 60°C - 260°C, the water content of the silk films can be determined.[33]

Our results revealed that silk film water content decreases with increasing MeOH-annealing concentration (Figure 5a). The water content of 30%, 40%, 50%, and 60% MeOH-annealed films were approximately 64%, 52%, 33%, and 15%, respectively. The primary peaks of the TGA first derivative mass loss profiles were also assessed to determine the rate of

evaporative mass loss (Figure 5b). Peak evaporation rate was reached at higher temperatures as the MeOH-annealing concentrations decrease. This suggests that softer films annealed with lower MeOH concentrations are able to both hold more water and may be more resistant to evaporation than stiffer films. Due to the air-liquid interface of the corneal environment, evaporation can be a concern, particularly if a corneal wound disrupts the integrity of the tear film.[51, 52] Silk films with greater water retention may be able to limit the effects of evaporation and subsequent complications such as dry eye. Overall, our FTIR and TGA results are consistent with the literature and confirm our hypotheses that β-sheet density and water content are both associated with the stiffness of silk films.

3.4. Methanol annealing changes the topographical cues present at the surface of silk films

It is known that changes in polymer crosslinking can directly affect the surface topography of biomaterials [53, 54] and thus can alter the biophysical cues at the cell-material interface. Like stiffness, topographical features of a material's surface can also alter cell behaviors critical for wound healing. Work from our group has demonstrated that corneal epithelial cell adhesion, migration, and expression of stem cell markers can be strongly influenced by patterned silk film surfaces.[5–8] We thus sought to use AFM to assess and quantify the surface topography of our silk films to better understand how it can be altered by MeOH processing. For this, AFM was operated in liquid, non-contact mode with silk films immersed in PBS. SEM imaging was additionally performed for visual comparison. It should be noted that ethanol dehydration was used for the preparation of silk films for SEM. While ethanol has been shown to induce β-sheets in the fibroin polymer, though less efficiently than MeOH,[55–57] all samples were fixed prior to ethanol exposure. Nevertheless, SEM images were used only for comparison and only AFM topographies were quantified. To our knowledge, this is the first AFM study to characterize the surface topography of fully hydrated silk films in an aqueous environment. Both AFM and SEM images reveal that silk fibroin particles decreased in size and appeared more densely packed as MeOH-annealing concentrations increased (Figure 6). For instance, films annealed with 30% MeOH visually appear "rougher" with larger surface topography when compared to 60% films.

In order to quantify their topographies, each film's respective AFM profiles were evaluated using Fourier power spectral analysis (Figure 7). Power spectral analysis allows for the quantification of both the vertical and lateral dimensions of topography, while conventional methods are usually limited to only vertical dimensions.[58] After fitting the ABC model (Equation 1) to the power spectral densities (PSD) of each film, the root-mean-square (RMS) was calculated (Equation 2) to represent the vertical topography, while the correlation length, which can be thought of as the average grain size, was calculated (Equation 3) to represent the horizontal topography.[58, 59]

$$PSD_{ABC} = \frac{A}{\left(1 + B^2 f^2\right)^{C + 1/2}} \quad (1)$$

$$\sigma_{ABC}^2 = \frac{2\pi A}{B^2(C-1)} \quad , \quad \tau_{ABC}^2 = \frac{(C-1)^2 B^2}{2\pi^2 C} \tag{2, 3}$$

The results shown in Table 1 reveal that the dimensions of vertical and horizontal topographies vary on different magnitudes; vertical topography varies on a nanometer scale, while lateral topography varies on a micrometer scale. When comparing the vertical topographies, the RMS roughness of MeOH-annealed films decreased from 14.38 nm to 8.51 nm with increasing MeOH concentrations. Comparison of the horizontal topographies using the correlation length also showed a decrease in grain size with increasing MeOH concentrations, from 2.54 μm to 0.57 μm. Overall, this indicates that the roughness of silk film surfaces decreases as MeOH-annealing concentrations increase, though the width of the topographical features is more strongly affected than its depth.

Cell response to topography is complex and seemingly cell-type dependent. Liliensiek et al. revealed that corneal epithelial cell proliferation was inhibited on nanoscale topography with features sizes similar to those of the corneal basement membrane, while corneal fibroblast proliferation was largely unaffected.[60] Kim et al. demonstrated that mammary epithelial cell adhesion and spreading were increased on moderately rough surfaces, but were inhibited when surface roughness became excessive.[61] To further complicate the matter, a separate study by Fraser et al. showed that alignment of primary corneal epithelial cells along surface patterns depended on the aspect ratio of horizontal and vertical dimensions of its surface features.[62] These studies highlight the complexities of the cellular response to material topographies and indicate the difficulty in predicting potential effects of specific topographies on cell behavior. Though previous work from our own group has demonstrated that lithography-patterned silk films could promote corneal epithelial cell wound healing,[5–8] the topography of the MeOH-annealed films are random and unpatterned and therefore cannot be directly compared. However, we believe that due to the much greater width and the relatively shallow vertical dimensions of the film topographies, the apparent roughness of the films is reduced. We thus speculate that corneal cell behavior will not be greatly influenced by differences in surface topography, though the rougher 30% MeOH-annealed films may have a greater effect than the other films. Nevertheless, both qualitative and quantitative results reveal that MeOH-anneal does indeed alter the topographical cues present at the surfaces of silk films, and therefore, may affect cellular mechanosignaling.

3.5. Corneal epithelial cell mechanosignaling can be controlled using methanol-annealed silk films

After developing a method to tune the stiffness of silk films and to characterize their surface mechanical properties in an aqueous environment, we next sought to determine whether human corneal epithelial cells are sensitive to the mechanical cues present on the films. We chose to investigate common markers of cellular mechanosensing that include cell spreading area, actin cytoskeletal tension, and the localization of the transcriptional co-activator Yes-associated protein (YAP). YAP is a well-recognized cellular mechanotransducer of substrate stiffness.[63] While the exact mechanisms are still unclear, it is known that on stiff matrices that promote cell spreading and increased actin cytoskeletal tension, unphosphorylated YAP

translocates into the cellular nucleus. Once in the nucleus, YAP acts as a cofactor for the transcriptional regulators TEAD, SMAD, or Runx. Conversely, on soft matrices that suppress intracellular contractile forces, phosphorylated YAP is sequestered in the cytoplasm where it is targeted for degradation.[64–66] Recent studies by Gouveia et al. have begun to reveal the importance of matrix stiffness and the role of YAP in the maintenance of limbal epithelial stem cells and the corneal epithelium.[16, 67]

We used the human corneal limbal epithelial (HCLE) cell line as a model for assessing the mechanosensitivity of corneal epithelial cells (Figure 8). Phase-contrast images show observable differences in HCLE cell size when cultured on film of different MeOH-annealing concentrations (Figure 8a). Quantification revealed that the average cell area on the soft, 13.4 kPa films (30%) was significantly smaller compared to cells cultured on the stiff, 445.4 kPa films (60%) (Figure 8b).

While cell areas were not statistically significant when comparing other films, we observed a steady increase in cell size as HCLE cells were cultured on stiffer films. We next evaluated whether YAP nuclear localization is affected by silk film mechanical properties. HCLE cells cultured on silk films were fixed and immunostained to reveal differences in cytoskeletal and YAP distribution (Figure 9).

To quantify YAP localization, HCLE cells were categorized based on their distribution of YAP signal according to methods published by multiple groups.[34–37] Results are represented as a percentage of the cell population exhibiting predominantly nuclear YAP distribution. We observed that YAP nuclear localization was significantly reduced in HCLE cells grown on soft, 13.4 kPa films (30%) compared to those on stiff, 445.4 kPa films (60%). While statistically there was no significance between other MeOH film concentrations, we observed an increasing trend of the percentage of the cell population displaying nuclear YAP localization as the film stiffness increased (Figure 9a–b). This trend compares closely with that of the cell area measurements in Figure 8, corroborating that YAP nuclear localization is closely associated with cell size and that both are affected by substrate stiffness. Further immunostaining with fluorescence-labeled phalloidin revealed that actin stress fibers were more prominent in cells cultured on the stiffer 128.9 kPa (50%) and 445.4 kPa (60%) films compared to those grown on softer 13.4 kPa (30%) and 40.9 kPa (40%) films (Figure 9a), indicating an increase in actin cytoskeletal tension. Overall, these findings indicate that corneal epithelial cells are indeed mechanosensitive to the stiffness changes present on silk film surfaces annealed with different concentrations of MeOH.

3.6. Silk Film Stiffness Correlates with Corneal Epithelial Cell Area

While initially, our goal was to elucidate the effects of silk film stiffness on corneal epithelial mechanosignaling, the contribution of surface topography cannot be ruled out. Though YAP mechanotransduction is largely associated with stiffness mechanosensing, studies have demonstrated that surface topography can also influence YAP signaling.[68–70] We thus sought to determine whether silk film stiffness or surface topography contributed more to the observed changes in corneal epithelial cell morphology. For this, simple linear regression was performed with cell area as the dependent variable and with the log of the

Young's modulus, RMS roughness, and correlation length each as independent variables (Table 2).

Our analyses revealed that only the Young's modulus was significantly correlated with corneal epithelial cell area ($R^2 = 0.96$, $p < 0.05$). No significance was found with the RMS roughness ($p = 0.056$) or correlation length ($p = 0.17$), although the RMS roughness approached significance. This suggests that cell spreading area, and consequently YAP mechanosignaling, is more closely related to the stiffness of silk films rather than to either vertical or horizontal dimensions of surface topography. Our analysis, however, was limited by the degrees of freedom, and multiple linear regression with all three independent variables could not be performed. While the Young's modulus is the predominant factor influencing cell mechanosensing in our analysis, the surface topography, particularly the RMS roughness, likely also has some contribution to both cell size and cytoskeletal tension. Nevertheless, our results suggest that the stiffness of MeOH-annealed silk films is the primary mechanical property affecting corneal epithelial cell mechanosignaling. This is the first study investigating the tunability of silk film stiffness within the range of physiologic corneal tissue for the purposes of regulating corneal epithelial cell mechanosignaling.

4. CONCLUSION

Films cast from the silk fibroin solution are promising biomaterial candidates for corneal tissue engineering. The tunability of their mechanical properties opens the possibility of engineering a physical microenvironment that better resembles that of the native corneal tissue. Here, we demonstrated that the stiffness of silk fibroin films can be manipulated over a wide range using simple MeOH processing. AFM was used to characterize film surfaces in an aqueous environment and provide insight into the biophysical cues present at the cell-material interface. Our AFM results indicated that silk film stiffness increased considerably with the MeOH concentration used for annealing, and Young's moduli spanning 13.4 ± 5.4 kPa to 445.4 ± 138.7 kPa were achieved with MeOH concentrations between 30–60%. These results also revealed that the surface stiffness of these films is considerably lower than that of their bulk when compared to studies reported by other groups. Further mechanical characterization demonstrated that water content decreased with greater MeOH concentrations while β-sheet structures increased. Analysis and quantification of the surface topographies revealed that the films decreased in roughness as MeOH concentrations increased. HCLE cells cultured on silk films with different stiffness displayed clear indicators of mechanosignaling including differences in cell spreading area, YAP nuclear localization, and increased actin cytoskeletal tension. Finally, simple linear regression revealed that cell spreading area was influenced predominantly by the Young's modulus of the films. This study demonstrates how the mechanical stiffness of silk fibroin films can be tuned to resemble that of the native corneal tissue and that corneal epithelial cells are mechanosensitive within this stiffness range. Future work will explore how the mechanical cues of silk fibroin films can be used to promote corneal wound regeneration, limbal stem cell maintenance, and integration within corneal tissue.

ACKNOWLEDGEMENTS

This work was supported by National Institutes of Health (Grant Nos. K12EY021475, R21EY019561, R01EY027912, and P30EY001792); the Medical Scientist Training Program Predoctoral Training Grant (Grant No. T32GM079086); the Illinois Society for the Prevention of Blindness (Grant No. 097371); the Research to Prevent Blindness Unrestricted Departmental Grant; and the Falk Medical Research Trust Catalyst Awards Program. The authors would also like to thank both the Nanocore Facility and the Electron Microscopy Core at the University of Illinois at Chicago for providing help with the thermogravimetric analyses and scanning electron microscopy, respectively. Additionally, the authors thank Dr. David Eddington for providing access to their oxygen plasma vacuum system. Finally, the authors would like to thank Dr. Ilene Gipson for kindly providing the HCLE cells.

References

1. Ghezzi CE, Marelli B, Omenetto FG, Funderburgh JL, Kaplan DL. PLoS One. 2017, 12, e0169504. [PubMed: 28099503]
2. Gosselin EA, Torregrosa T, Ghezzi CE, Mendelsohn AC, Gomes R, Funderburgh JL, Kaplan DL. J Tissue Eng Regen Med 2018, 12, 285–95. [PubMed: 28600807]
3. Jia L, Ghezzi CE, Kaplan DL. Journal of Biomedical Materials Research Part B: Applied Biomaterials. 2016, 104, 431–41.
4. Kim EY, Tripathy N, Cho SA, Joo C-K, Lee D, Khang G. Colloids and Surfaces B: Biointerfaces. 2015, 136, 394–401. [PubMed: 26433646]
5. Kang KB, Lawrence BD, Gao XR, Guaiquil VH, Liu A, Rosenblatt MI. Sci Rep 2019, 9, 1507. [PubMed: 30728382]
6. Kang KB, Lawrence BD, Gao XR, Luo Y, Zhou Q, Liu A, Guaiquil VH, Rosenblatt MI. Invest Ophthalmol Vis Sci 2017, 58, 6388–98. [PubMed: 29260198]
7. Lawrence BD, Pan Z, Rosenblatt MI. PLoS One. 2012, 7, e50190. [PubMed: 23185573]
8. Lawrence BD, Pan Z, Weber MD, Kaplan DL, Rosenblatt MI. J Vis Exp 2012,
9. Keller R, Davidson LA, Shook DR. Differentiation. 2003, 71, 171–205. [PubMed: 12694202]
10. Engler AJ, Sen S, Sweeney HL, Discher DE. Cell. 2006, 126, 677–89. [PubMed: 16923388]
11. Chen S, Shi J, Xu X, Ding J, Zhong W, Zhang L, Xing M, Zhang L. Colloids and Surfaces B: Biointerfaces. 2016, 140, 574–82. [PubMed: 26628331]
12. Moshayedi P, Ng G, Kwok JC, Yeo GS, Bryant CE, Fawcett JW, Franze K, Guck J. Biomaterials. 2014, 35, 3919–25. [PubMed: 24529901]
13. Wu L, Magaz A, Darbyshire A, Howkins A, Reynolds A, Boyd IW, Song H, Song J-H, Loizidou M, Emberton M, Birchall M, Song W. Advanced Healthcare Materials. 2019, 8, 1801556.
14. Levental KR, Yu H, Kass L, Lakins JN, Egeblad M, Erler JT, Fong SF, Csiszar K, Giaccia A, Weninger W, Yamauchi M, Gasser DL, Weaver VM. Cell. 2009, 139, 891–906. [PubMed: 19931152]
15. Paszek MJ, Zahir N, Johnson KR, Lakins JN, Rozenberg GI, Gefen A, Reinhart-King CA, Margulies SS, Dembo M, Boettiger D, Hammer DA, Weaver VM. Cancer Cell. 2005, 8, 241–54. [PubMed: 16169468]
16. Gouveia RM, Lepert G, Gupta S, Mohan RR, Paterson C, Connon CJ. Nat Commun 2019, 10, 1496. [PubMed: 30944320]
17. Roach P, Eglin D, Rohde K, Perry C. Journal of materials science Materials in medicine. 2007, 18, 1263–77. [PubMed: 17443395]
18. Mizuno HL, Tan E, Anraku Y, Sakai T, Sakuma I, Akagi Y. Langmuir 2020, 36, 5554–62. [PubMed: 32365299]
19. Amani H, Arzaghi H, Bayandori M, Dezfuli AS, Pazoki-Toroudi H, Shafiee A, Moradi L. Adv Mater Interfaces. 2019, 6, 1900572.
20. Beckstead BL, Santosa DM, Giachelli CM. Journal of Biomedical Materials Research Part A. 2006, 79A, 94–103.
21. Puleo DA, Nanci A. Biomaterials. 1999, 20, 2311–21. [PubMed: 10614937]
22. Shen Y, Gao M, Ma Y, Yu H, Cui F.-z., Gregersen H, Yu Q, Wang G, Liu X. Colloids and Surfaces B: Biointerfaces. 2015, 126, 188–97. [PubMed: 25575348]

23. Zhang X, Bao H, Donley C, Liang J, Yang S, Xu S. BMC Chem 2019, 13, 62. [PubMed: 31384810]
24. Sheik S, Sheik S, Nairy R, Nagaraja GK, Prabhu A, Rekha PD, Prashantha K. Int J Biol Macromol 2018, 116, 45–53. [PubMed: 29733927]
25. Sengupta S, Park SH, Seok GE, Patel A, Numata K, Lu CL, Kaplan DL. Biomacromolecules. 2010, 11, 3592–9. [PubMed: 21105641]
26. Lu Q, Zhang B, Li M, Zuo B, Kaplan DL, Huang Y, Zhu H. Biomacromolecules. 2011, 12, 1080–6. [PubMed: 21361368]
27. Jiang C, Wang X, Gunawidjaja R, Lin Y-H, Gupta MK, Kaplan DL, Naik RR, Tsukruk VV. Advanced Functional Materials. 2007, 17, 2229–37.
28. Galeotti F, Andicsová A, Bertini F, Botta C. J Mater Sci 2013, 48, 7004–10.
29. Servoli E, Maniglio D, Motta A, Predazzer R, Migliaresi C. Macromolecular Bioscience. 2005, 5, 1175–83. [PubMed: 16315185]
30. Vesel A, Junkar I, Cvelbar U, Kovac J, Mozetic M. Surf Interface Anal 2008, 40, 1444–53.
31. Hu X, Kaplan D, Cebe P. Macromolecules. 2006, 39, 6161–70.
32. Hu X, Shmelev K, Sun L, Gil ES, Park SH, Cebe P, Kaplan DL. Biomacromolecules. 2011, 12, 1686–96. [PubMed: 21425769]
33. Lawrence BD, Wharram S, Kluge JA, Leisk GG, Omenetto FG, Rosenblatt MI, Kaplan DL. Macromol Biosci 2010, 10, 393–403. [PubMed: 20112237]
34. Totaro A, Castellan M, Battilana G, Zanconato F, Azzolin L, Giulitti S, Cordenonsi M, Piccolo S. Nat Commun 2017, 8, 15206. [PubMed: 28513598]
35. Szeto SG, Narimatsu M, Lu M, He X, Sidiqi AM, Tolosa MF, Chan L, De Freitas K, Bialik JF, Majumder S, Boo S, Hinz B, Dan Q, Advani A, John R, Wrana JL, Kapus A, Yuen DA. Journal of the American Society of Nephrology : JASN. 2016, 27, 3117–28. [PubMed: 26961347]
36. Beamish JA, Chen E, Putnam AJ. PloS one. 2017, 12, e0181085–e. [PubMed: 28715434]
37. Jia Q, Zhou W, Yao W, Yang F, Zhang S, Singh R, Chen J, Chen JJ, Zhang Y, Wei F, Zhang Y, Jia H, Wang N. Oncogenesis. 2016, 5, e220–e. [PubMed: 27089143]
38. Inagaki N, Narushima K, Lim SK. J Appl Polym Sci 2003, 89, 96–103.
39. Lee JH, Khang G, Lee JW, Lee HB. J Colloid Interface Sci 1998, 205, 323–30. [PubMed: 9735195]
40. Brusatin G, Panciera T, Gandin A, Citron A, Piccolo S. Nature Materials. 2018, 17, 1063–75. [PubMed: 30374202]
41. Wu X, Wu X, Yang B, Shao M, Feng G. Appl Spectrosc 2017, 71, 1785–94. [PubMed: 28537487]
42. Last JA, Thomasy SM, Croasdale CR, Russell P, Murphy CJ. Micron 2012, 43, 1293–8. [PubMed: 22421334]
43. Labate C, De Santo MP, Lombardo G, Lombardo M. PLOS ONE. 2015, 10, e0122868. [PubMed: 25830534]
44. Lombardo M, Lombardo G, Carbone G, De Santo MP, Barberi R, Serrao S. Investigative Ophthalmology & Visual Science. 2012, 53, 1050–7. [PubMed: 22266511]
45. Xia D, Zhang S, Hjortdal JØ, Li Q, Thomsen K, Chevallier J, Besenbacher F, Dong M. ACS Nano. 2014, 8, 6873–82. [PubMed: 24833346]
46. Antons J, Marascio MGM, Nohava J, Martin R, Applegate LA, Bourban PE, Pioletti DP. J Mater Sci Mater Med 2018, 29, 57. [PubMed: 29728770]
47. Peng G, McNary SM, Athanasiou KA, Reddi AH. Tissue engineering Part A. 2014, 20, 3332–41. [PubMed: 24947008]
48. Darling EM, Wilusz RE, Bolognesi MP, Zauscher S, Guilak F. Biophys J 2010, 98, 2848–56. [PubMed: 20550897]
49. Lu Q, Hu X, Wang X, Kluge JA, Lu S, Cebe P, Kaplan DL. Acta Biomater 2010, 6, 1380–7. [PubMed: 19874919]
50. Hu X, Kaplan D, Cebe P. Macromolecules. 2008, 41, 3939–48.
51. Seo J, Byun WY, Alisafaei F, Georgescu A, Yi Y-S, Massaro-Giordano M, Shenoy VB, Lee V, Bunya VY, Huh D. Nat Med 2019, 25, 1310–8. [PubMed: 31384041]

52. Wong AHY, Cheung RKY, Kua WN, Shih KC, Chan TCY, Wan KH. Asia Pac J Ophthalmol (Phila). 2019, 8, 397–405. [PubMed: 31490199]
53. Rizwan M, Peh GSL, Ang HP, Lwin NC, Adnan K, Mehta JS, Tan WS, Yim EKF. Biomaterials. 2017, 120, 139–54. [PubMed: 28061402]
54. Fiejdasz S, Horak W, Lewandowska-Łańcucka J, Szuwarzyński M, Salwiński J, Nowakowska M. Journal of Colloid and Interface Science. 2018, 524, 102–13. [PubMed: 29635083]
55. Jin H-J, Park J, Karageorgiou V, Kim U-J, Valluzzi R, Cebe P, Kaplan DL. Advanced Functional Materials. 2005, 15, 1241–7.
56. Kaewpirom S, Boonsang S. RSC Advances. 2020, 10, 15913–23.
57. Nogueira GM, Rodas ACD, Leite CAP, Giles C, Higa OZ, Polakiewicz B, Beppu MM. Bioresource Technology. 2010, 101, 8446–51. [PubMed: 20598877]
58. Gong Y, Misture ST, Gao P, Mellott NP. The Journal of Physical Chemistry C. 2016, 120, 22358–64.
59. Tokas RB, Jena S, Thakur S, Sahoo NK. Thin Solid Films. 2016, 609, 42–8.
60. Liliensiek SJ, Campbell S, Nealey PF, Murphy CJ. Journal of Biomedical Materials Research Part A. 2006, 79A, 185–92.
61. Kim M-H, Kino-oka M, Kawase M, Yagi K, Taya M. Journal of Bioscience and Bioengineering. 2007, 103, 192–9. [PubMed: 17368404]
62. Fraser SA, Ting Y-H, Mallon KS, Wendt AE, Murphy CJ, Nealey PF. Journal of Biomedical Materials Research Part A. 2008, 86A, 725–35.
63. Dupont S, Morsut L, Aragona M, Enzo E, Giulitti S, Cordenonsi M, Zanconato F, Le Digabel J, Forcato M, Bicciato S, Elvassore N, Piccolo S. Nature. 2011, 474, 179–83. [PubMed: 21654799]
64. Hou Y, Xie W, Yu L, Camacho LC, Nie C, Zhang M, Haag R, Wei Q. Small. 2020, 16, e1905422. [PubMed: 32064782]
65. Huang J, Peng X, Xiong C, Fang J. J Colloid Interface Sci 2011, 355, 503–8. [PubMed: 21232749]
66. Yeung T, Georges PC, Flanagan LA, Marg B, Ortiz M, Funaki M, Zahir N, Ming W, Weaver V, Janmey PA. Cell Motil Cytoskeleton. 2005, 60, 24–34. [PubMed: 15573414]
67. Gouveia RM, Vajda F, Wibowo JA, Figueiredo F, Connon CJ. Cells. 2019, 8,
68. Raghunathan VK, Dreier B, Morgan JT, Tuyen BC, Rose BW, Reilly CM, Russell P, Murphy CJ. PloS one. 2014, 9, e109811–e. [PubMed: 25290150]
69. Zhang Y, Gong H, Sun Y, Huang Y, Fan Y. Journal of Biomedical Materials Research Part A. 2016, 104, 1143–52. [PubMed: 26748630]
70. Mascharak S, Benitez PL, Proctor AC, Madl CM, Hu KH, Dewi RE, Butte MJ, Heilshorn SC. Biomaterials. 2017, 115, 155–66. [PubMed: 27889666]

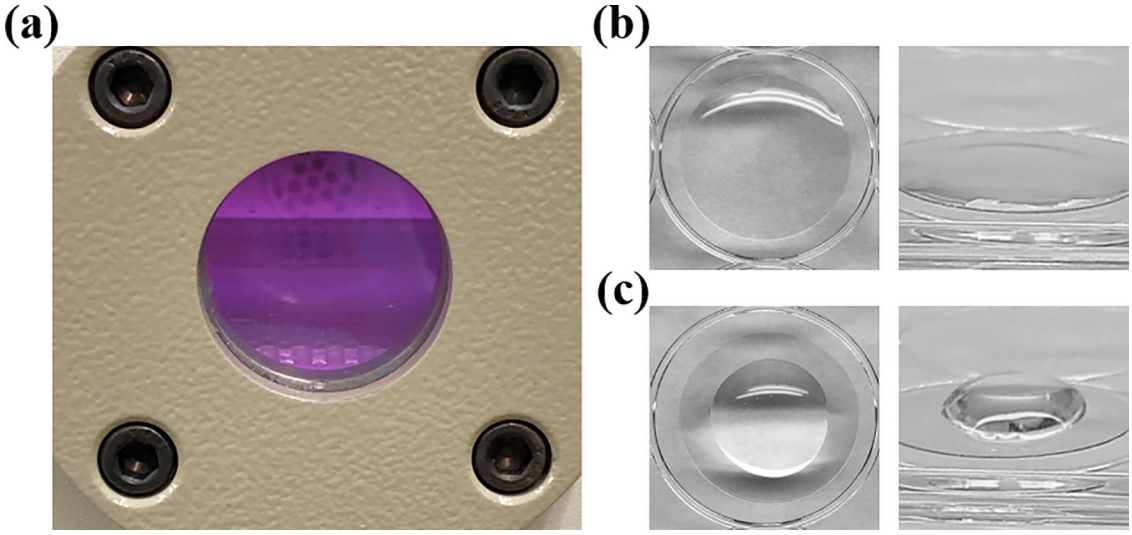

Figure 1.

Oxygen plasma increases the surface energy of polyester, allowing for bonding with the silk fibroin polymer. **(a)** Polyester coverslips are exposed to oxygen plasma within a vacuum for surface activation. **(b)** Silk fibroin solution is cast directly onto plasma-treated coverslips. Plasma-activated polyester is hydrophilic and facilitates spreading of aqueous silk solution. **(c)** In contrast, untreated polyester is hydrophobic and resists spreading of the fibroin solution.

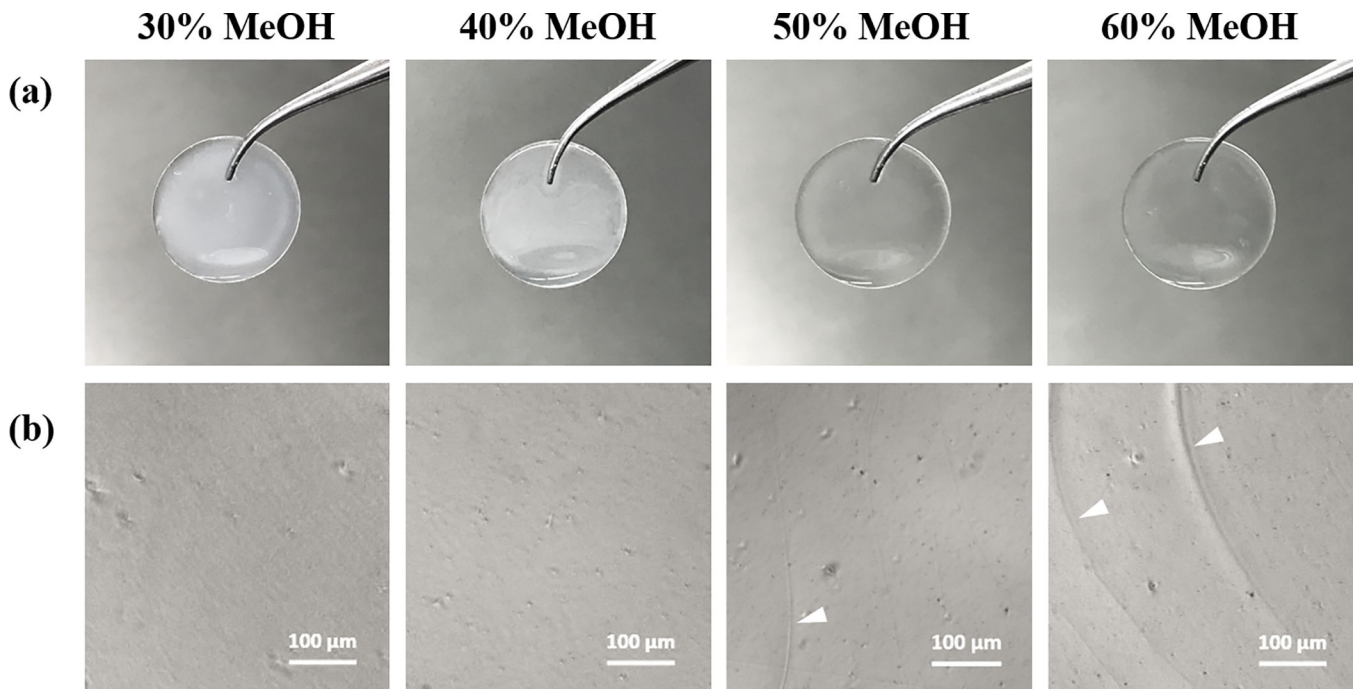

Figure 2.

Silk fibroin films annealed with 30%, 40%, 50% and 60% MeOH and hydrated in PBS. **(a)** Examples of MeOH-annealed films cast on plasma-treated plastic cover slips. Optical transparency of films visually improves as MeOH-annealing concentration increases. **(b)** Phase-contrast images of MeOH-annealed silk films. Cracks can be seen in 50% and 60% films and indicate embrittlement induced by higher concentration MeOH-annealing (white arrowheads).

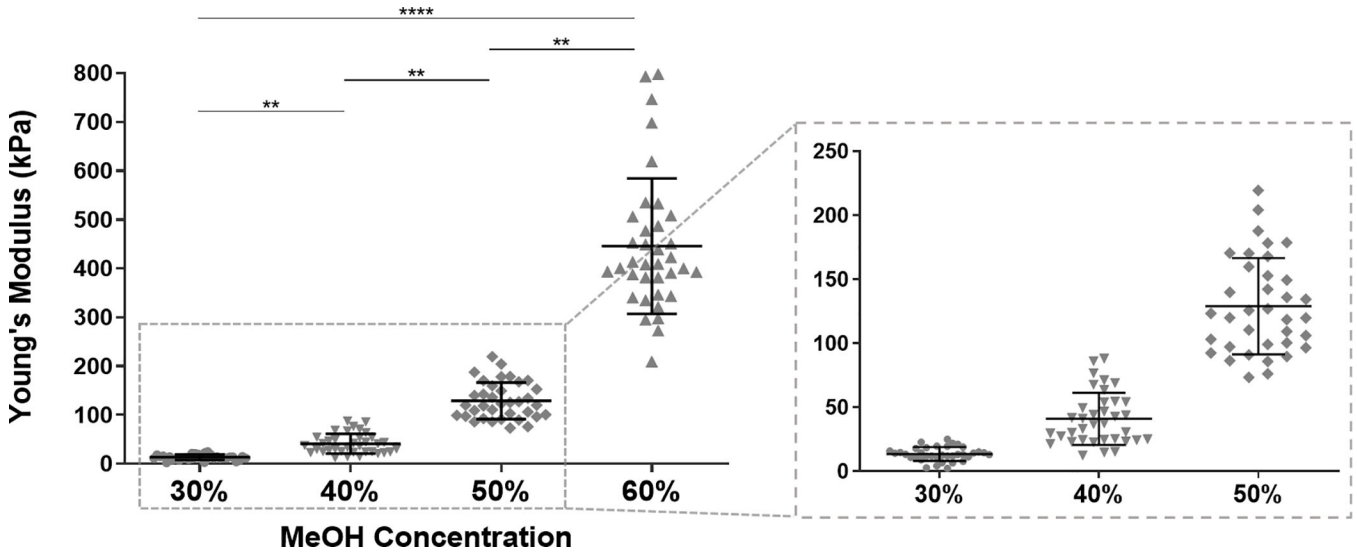

Figure 3.

Young's moduli of 30%, 40%, 50% and 60% MeOH-annealed silk films measured by AFM nanoindentation. Data was fit with linear elastic Hertzian contact model to approximate values of elastic moduli. A portion of the graph is magnified for better visualization of data for 30%, 40% and 50% films (data is represented as individual measurements with mean ± SD from three separate samples per condition. **$p < 0.01$, ****$p < 0.0001$).

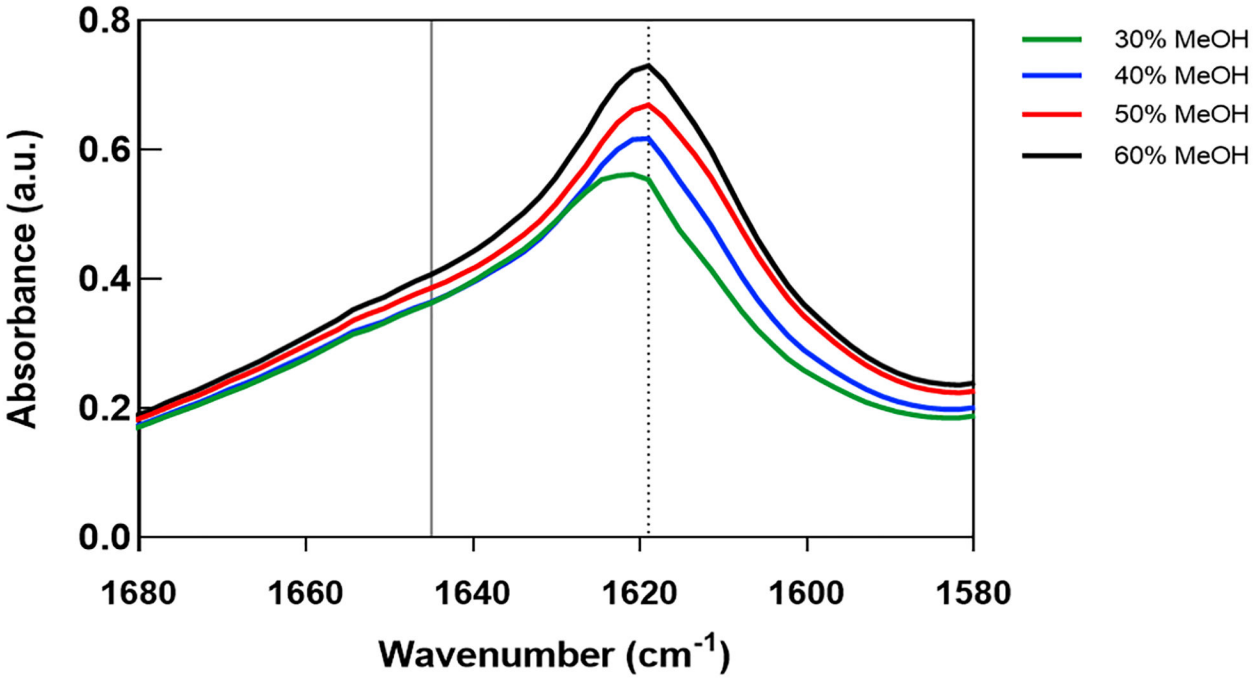

Figure 4.

Secondary structures of MeOH-annealed silk fibroin films analyzed with FTIR-ATR. β-sheet (1610–1625 cm^{-1}) and random-coil (1640–1650 cm^{-1}) structures are indicated by dashed and solid vertical lines, respectively. FTIR spectral data for 30%, 40%, 50%, and 60% MeOH-annealed silk films. Peak heights corresponding to β-sheet structures increase with greater MeOH-annealing concentrations.

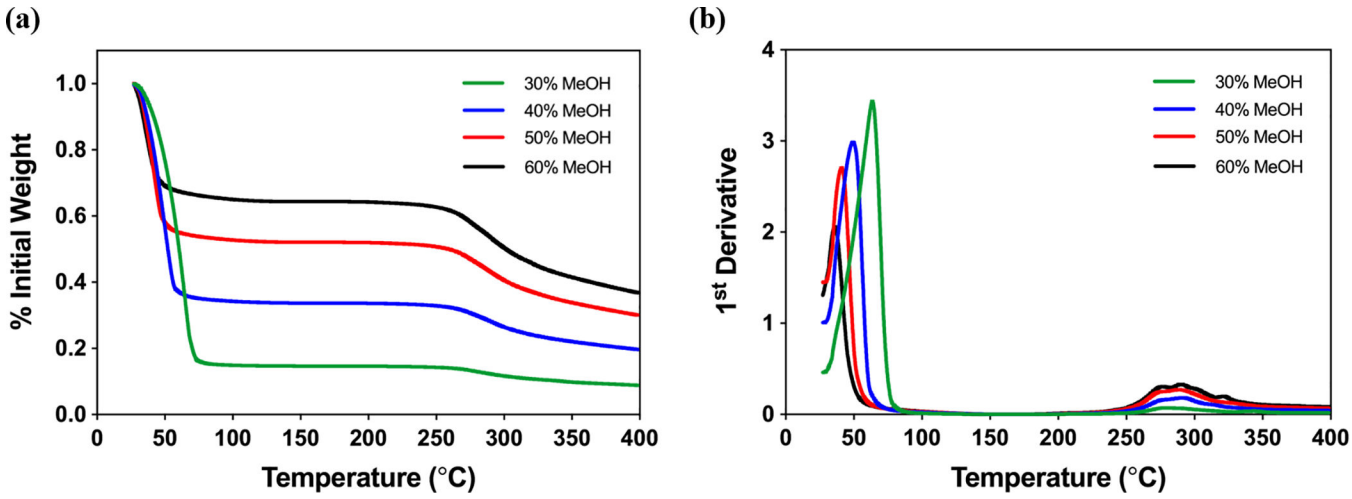

Figure 5.

Water content of MeOH-annealed silk fibroin films analyzed with TGA. **(a)** TGA mass loss profiles with respect to temperature for 30%, 40%, 50%, and 60% MeOH-annealed silk films hydrated in dH_2O. Initial plateau between 50°C-275°C corresponds to the mass remaining after water loss due to evaporation. Water content of films increases with decreasing MeOH concentrations. **(b)** TGA 1^{st} derivative profiles for MeOH-annealed silk films. Primary peaks correspond to rate of evaporative mass loss while secondary peaks indicate material degradation.

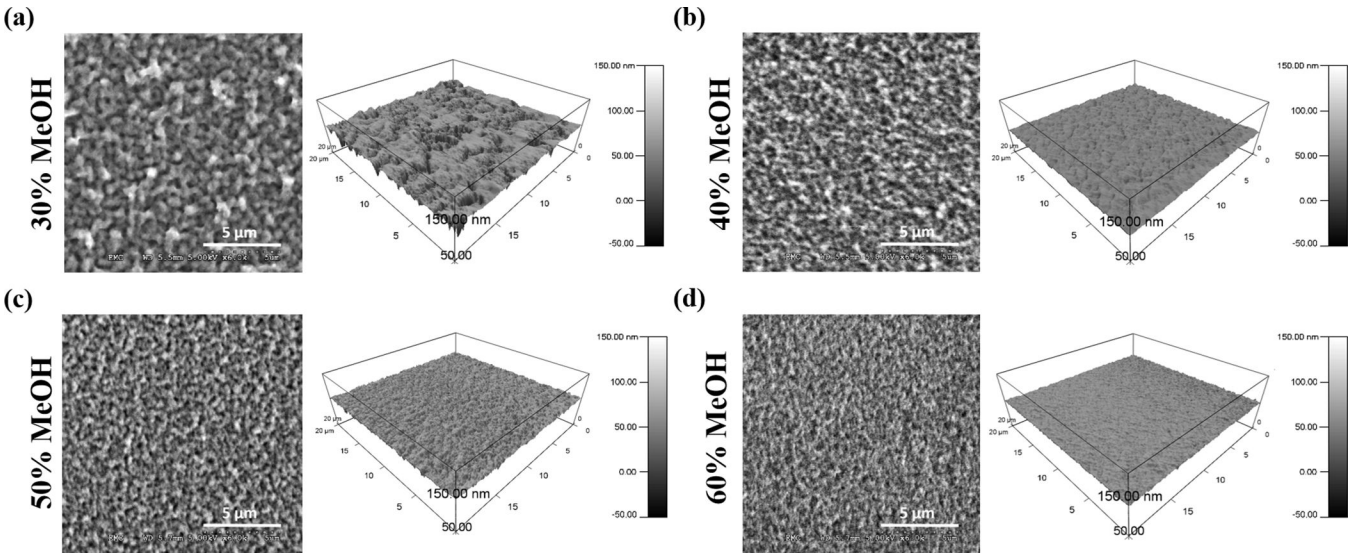

Figure 6.

Topography of MeOH-annealed silk films imaged with SEM and AFM. 2D images on the left correspond to dehydrated films imaged with SEM, while 3D images on the right correspond to hydrated films measured with AFM for **(a)** 30% MeOH-annealed **(b)** 40% MeOH-annealed **(c)** 50% MeOH-annealed and **(d)** 60% MeOH-annealed silk films. As MeOH-annealing concentration increases, silk particles become smaller and more densely packed.

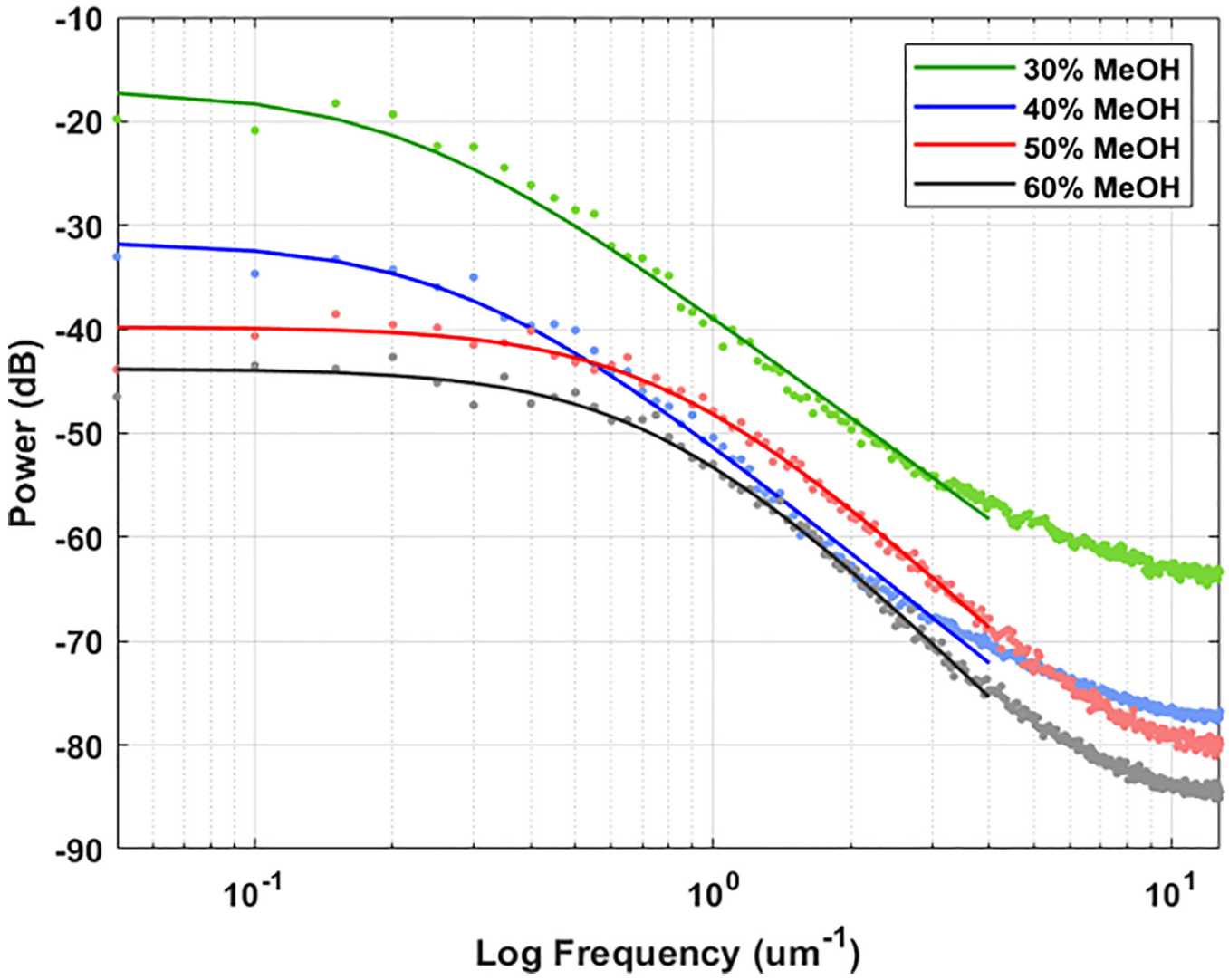

Figure 7.

Power spectral density of 30%, 40%, 50%, and 60% MeOH-annealed silk film topographies acquired from AFM data. The data was fitted with the ABC model (Eq.1), shown in the dashed lines, and the fitted A, B, and C coefficients were used to calculate the RMS roughness and correlation length of the film surfaces.

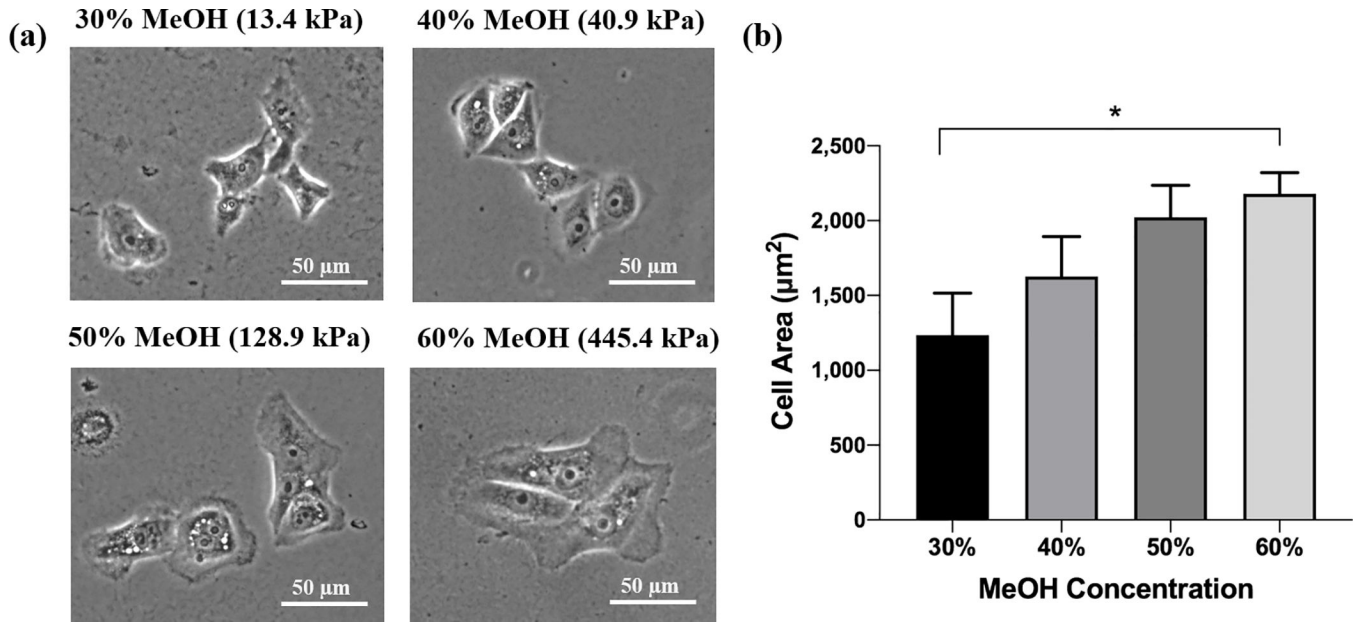

Figure 8.

HCLE cell spreading on MeOH-annealed silk films. **(a)** Phase-contrast images of HCLE cells cultured on 30%, 40%, 50% and 60% MeOH-annealed silk films. Cells appear larger with more prominent lamellipodia when cultured on films annealed with increasing MeOH concentration. **(b)** Quantification of cell areas via tracing (data is represented as mean ± 95% CI from three separate samples per condition. *$p < 0.05$).

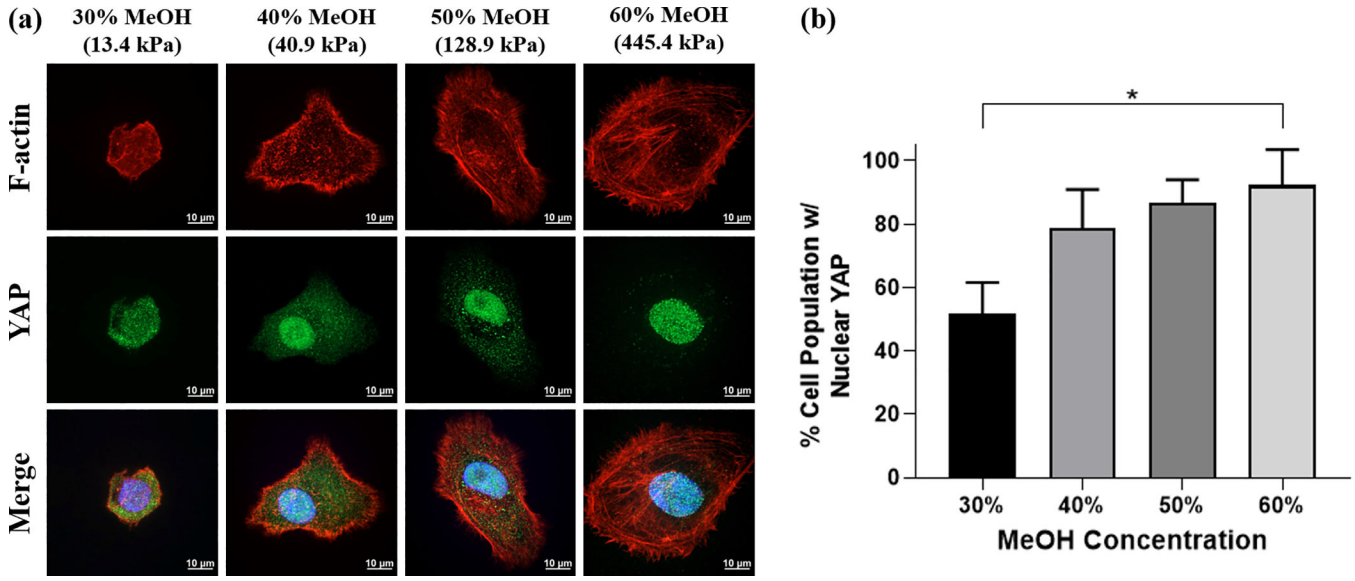

Figure 9.

Localization of molecular mechanotransducer YAP on MeOH-annealed silk films **(a)** Immunofluorescent staining of HCLE cells cultured on 30%, 40%, 50% and 60% MeOH-annealed silk films. Actin stress fibers labeled with phalloidin can be seen more prominently in cells grown on 50% and 60% films. Nuclear localization of YAP increases when cells are grown on stiffer films. **(b)** HCLE cells categorized by distribution of YAP. As cell are grown on stiffer silk films, a higher percentage of the cell population can be seen displaying predominantly nuclear YAP localization (data is represented as mean ± 95% CI. *$p < 0.05$ from three separate samples per condition).

Table 1.

ABC Model Fitting of Silk Film Surface Topography.

Sample	*A* [μm^3]	*B* [μm]	*C*	RMS Roughness [nm]	Correlation Length [μm]
30% MeOH	$7.21 \cdot 10^{-3}$	11.78	2.52	14.38	2.54
40% MeOH	$2.23 \cdot 10^{-3}$	9.04	2.72	10.28	1.98
50% MeOH	$1.17 \cdot 10^{-3}$	7.59	3.01	7.70	1.96
60% MeOH	$9.91 \cdot 10^{-5}$	1.67	4.17	8.51	0.57

Table 1. Fitting parameters acquired from the ABC model. The parameters were used to calculate the RMS roughness and correlation length for each silk film which describe the vertical and lateral features of a topography, respectively (values are represented as the mean of three independent experiments).

Table 2.

Linear Regression of Silk Film Mechanical Properties and Corneal Cell Area.

Model	Term	Coefficient	SE	T stat	P-value	R-square
Log Modulus vs. Cell Area	Intercept	576.72	178.87	3.22	0.084	
	Log Modulus	275.44	39.67	6.94	0.020	0.96
RMS Roughness vs. Cell Area	Intercept	3137.17	348.05	9.01	0.012	
	RMS Roughness	−134205.90	33020.57	−4.06	0.056	0.89
Correlation Length vs. Cell Area	Intercept	2506.10	380.19	6.59	0.022	
	Correlation Length	−419.64	199.28	−2.11	0.17	0.69

Table 2. Simple linear regression individually modeling the relationships between the independent variables and corneal epithelial cell area. The log of the Young's modulus, RMS roughness, and correlation length were chosen as the independent variables.